Journal of Power Sources 192 (2009) 652–659

Contents lists available at ScienceDirect

Journal of Power Sources

journal homepage: www.elsevier.com/locate/jpowsour

In situ X-ray diffraction studies of mixed $LiMn_2O_4$–$LiNi_{1/3}Co_{1/3}Mn_{1/3}O_2$ composite cathode in Li-ion cells during charge–discharge cycling

Kyung-Wan Nam[a], Won-Sub Yoon[b,*], Hyunjung Shin[b], Kyung Yoon Chung[c], Seungdon Choi[d], Xiao-Qing Yang[a]

[a] *Chemistry Department, Brookhaven National Laboratory, Upton, NY 11973, USA*
[b] *School of Advanced Materials Eng., Kookmin, Seoul 136-702, South Korea*
[c] *Battery Research Center, Korea Institute of Science and Technology, Seoul 136-791, South Korea*
[d] *Battery Research and Development, LG Chem. Research Park, Daejeon 305-380, South Korea*

ARTICLE INFO

Article history:
Received 17 January 2009
Received in revised form 26 February 2009
Accepted 26 February 2009
Available online 14 March 2009

Keywords:
Lithium battery
In situ XRD
Composite cathode
$LiMn_2O_4$
$LiNi_{1/3}Co_{1/3}Mn_{1/3}O_2$

ABSTRACT

The structural changes of the composite cathode made by mixing spinel $LiMn_2O_4$ and layered $LiNi_{1/3}Co_{1/3}Mn_{1/3}O_2$ in 1:1 wt% in both Li-half and Li-ion cells during charge/discharge are studied by *in situ* XRD. During the first charge up to ~5.2 V *vs.* Li/Li^+, the *in situ* XRD spectra for the composite cathode in the Li-half cell track the structural changes of each component. At the early stage of charge, the lithium extraction takes place in the $LiNi_{1/3}Co_{1/3}Mn_{1/3}O_2$ component only. When the cell voltage reaches at ~4.0 V *vs.* Li/Li^+, lithium extraction from the spinel $LiMn_2O_4$ component starts and becomes the major contributor for the cell capacity due to the higher rate capability of $LiMn_2O_4$. When the voltage passed 4.3 V, the major structural changes are from the $LiNi_{1/3}Co_{1/3}Mn_{1/3}O_2$ component, while the $LiMn_2O_4$ component is almost unchanged. In the Li-ion cell using a MCMB anode and a composite cathode cycled between 2.5 V and 4.2 V, the structural changes are dominated by the spinel $LiMn_2O_4$ component, with much less changes in the layered $LiNi_{1/3}Co_{1/3}Mn_{1/3}O_2$ component, comparing with the Li-half cell results. These results give us valuable information about the structural changes relating to the contributions of each individual component to the cell capacity at certain charge/discharge state, which are helpful in designing and optimizing the composite cathode using spinel- and layered-type materials for Li-ion battery research.

1. Introduction

The research and development of hybrid electric vehicle (HEV), plug-in hybrid electric vehicle (PHEV) and electric vehicle (EV) is intensified due to the energy crisis and environmental concerns. Having the highest energy density among all rechargeable batteries, lithium-ion battery is considered as one of the best candidates of rechargeable batteries for transportation applications. In order to meet the challenging requirements of powering HEV, PHEV and EV, the current lithium battery technology needs to be significantly improved in terms of the cost, safety, power and energy density, as well as the calendar and cycle life. One new technology being developed is the utilization of composite cathode by mixing two different types of insertion compounds [e.g., spinel $LiMn_2O_4$ and layered $LiMO_2$ (M = Ni, Co, and Mn)]. This new composite cathode has good potential to reduce cost and capacity fading, as well as the benefits of increased capacity and better safety characteristics. Several works have been reported on the mixed spinel $LiMn_2O_4$ and layered $LiMO_2$ composite cathode materials [1–6]. Other studies on the mixed $LiMPO_4$-type metal phosphates and layered $LiMO_2$ composite cathode materials were also reported [7,8]. Most of these works are focused on investigating the electrochemical properties and stability of the composite cathodes at high temperatures only and not much information on the Li insertion/extraction behaviors of each component in the composite cathode during charge/discharge has been reported. The *in situ* X-ray diffraction (XRD) is a powerful tool in providing valuable information about the Li insertion/extraction behaviors of each component in the composite cathode during charge/discharge cycling. Therefore, we applied the synchrotron-based *in situ* XRD technique to study the composite cathode and report the results in this paper.

The $LiMn_2O_4$ spinel is a good candidate as one component of the composite cathode material due to its low cost, low toxicity, fast kinetics and remarkable safety properties [9,10]. The new layered $LiNi_{1/3}Co_{1/3}Mn_{1/3}O_2$ cathode material is another good candidate due to its advantages in low cost, high specific capacity, and good thermal stability [11–14]. LG Chemical Corp. has been developing the composite cathode materials using these two

* Corresponding author. Tel.: +82 2 910 4664; fax: +82 2 910 4320.
E-mail addresses: wsyoon@kookmin.ac.kr, wsyoon@gmail.com (W.-S. Yoon).

0378-7753/$ – see front matter © 2009 Elsevier B.V. All rights reserved.
doi:10.1016/j.jpowsour.2009.02.088

components. In this paper, the results of the structural change studies of the $LiMn_2O_4$–$LiNi_{1/3}Co_{1/3}Mn_{1/3}O_2$ composite cathode during cycling in both half cell (Li metal anode) and Li-ion cell (mesocarbon microbeads, MCMB anode) using *in situ* synchrotron based XRD technique are reported. These results provide valuable information about the structural change behavior and different contributions of each individual component at certain charge/discharge state and are helpful in redesigning and optimizing the $LiMn_2O_4$–$LiNi_{1/3}Co_{1/3}Mn_{1/3}O_2$ composite cathode for Li-ion battery research.

2. Experimental

The $LiMn_2O_4$ and $LiNi_{1/3}Co_{1/3}Mn_{1/3}O_2$ powders were supplied by LG Chem. The spinel phase has little excess lithium (i.e., $Li_{1+y}Mn_{2-y}O_4$), but the exact composition is not available. The mixed oxide powders were prepared by mixing $LiMn_2O_4$ and $LiNi_{1/3}Co_{1/3}Mn_{1/3}O_2$ with 1:1 weight ratio in a mixer. Cathodes were prepared by slurring the active material powder with 10% poly-vinylidene fluoride (PVDF, KynarFlex 2801), and 10% acetylene black (w/w) in an n-methyl pyrrolidone (NMP) solvent, then coating the mixture onto Al foil. After drying at 100 °C for 12 h, the electrode disks (~2.8 cm^2) were punched and weighed. For the Li-half cell test, the cathodes were incorporated into *in situ* XRD cells with a metallic Li foil negative electrode and a Celgard separator. The electrolytes used were commercially available 1.2 M $LiPF_6$ in a 3:7 ethylene carbonate (EC)–ethyl methyl carbonate (EMC) solvents. For the Li-ion cell test, laminated pouch cells for *in situ* experiments were fabricated at LG Chem. using $LiMn_2O_4$–$LiNi_{1/3}Co_{1/3}Mn_{1/3}O_2$ (1:1 wt%) composite cathodes and MCMB anodes. The pouch cells were used in the *in situ* XRD measurements.

In situ XRD patterns were collected at the National Synchrotron Light Source (NSLS) at Brookhaven National Laboratory (BNL) using wide-angle position sensitive detector (PSD) at beamline X18A and Mar 345-image plate detector at X7B in the transmission mode. The wavelengths used were 0.9999 Å at X18A and 0.9212 Å at X7B. The PSD and Mar 345-image plate detector can cover 90° of 2θ angles simultaneously with a good signal to noise ratio, and thus collect one XRD scan in a period as short as a few minutes. It significantly reduced the data collection time for each scan, giving us a great advantage in studying the phase transition in real time. For easy comparison purpose, the 2θ angles of all the XRD patterns presented in this paper have been recalculated and converted to the corresponding angles for a λ = 1.54 Å, which is the wavelength of a conventional X-ray tube source with Cu-Kα radiation.

3. Results and discussion

The structural changes of each component in the $LiMn_2O_4$–$LiNi_{1/3}Co_{1/3}Mn_{1/3}O_2$ composite cathode are studied separately in

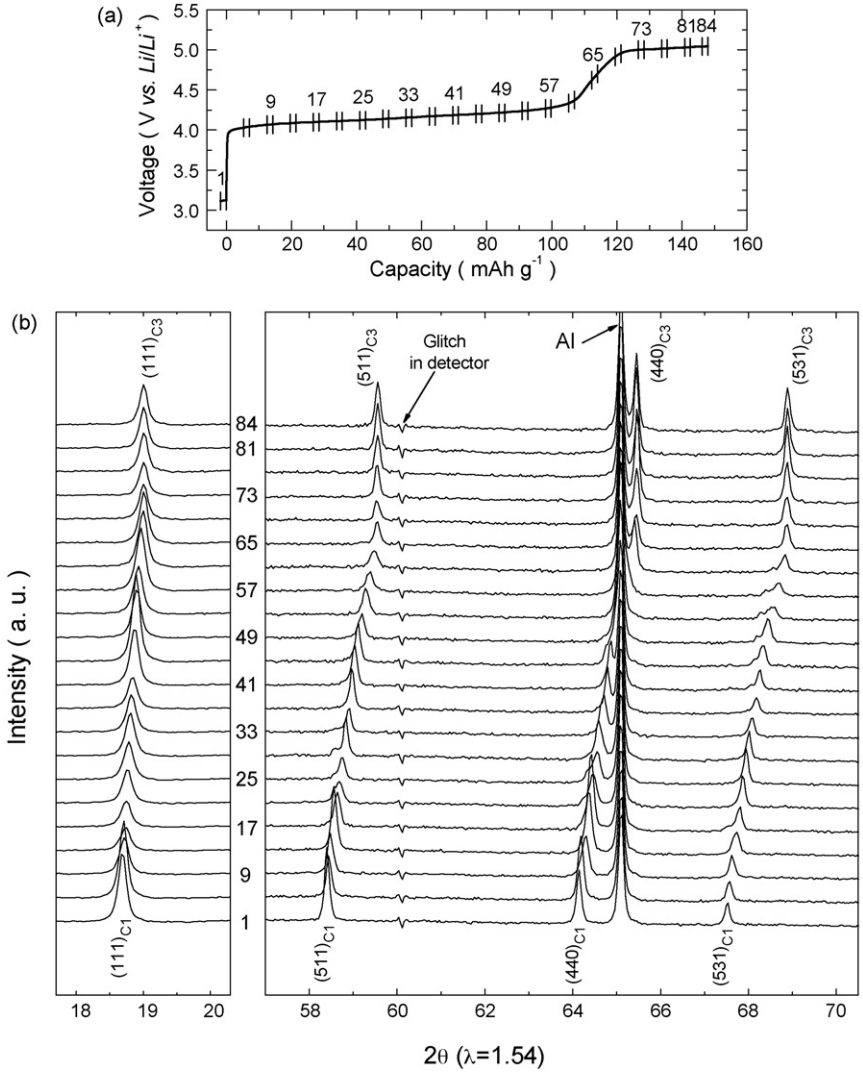

Fig. 1. (a) First charge curve of $LiMn_2O_4$ cathode in the Li-half cell at C/7 rate, and (b) corresponding *in situ* XRD patterns.

the half cell first. Fig. 1(a) shows the first charge curve of the $LiMn_2O_4$ cathode using a constant current at a C/7 rate. In order to get more complete information about the structural changes in a wide voltage range, a 5.0 V cut-off voltage was used. A single voltage plateau at ~4.0 V, rather than the typical two plateaus at 4.0 V and 4.1 V for $LiMn_2O_4$ was observed. This may be a result of the lithium rich nature of the spinel used by LG Chem. After charged to 4.2 V, the voltage increased rapidly to a value close to 5.0 V and stayed at that level until the end of charge. This is attributed to the electrolyte decomposition, which will be discussed later in this paper using the *in situ* XRD results. When charged to the voltage of 4.8 V, the charge capacity of the $LiMn_2O_4$ cathode is measured as 116 mAh g^{-1}. The *in situ* XRD patterns collected during the first charge are plotted in Fig. 1(b). During the first charge, a total of 84 XRD scans were continuously collected but only 22 XRD patterns are used in Fig. 1(b) with the corresponding scan number indicated above the charging curve in Fig. 1(a). The selected XRD scan numbers are labeled in Fig. 1(b). The scan 1 was collected before charge. All of the *in situ* XRD plots in this paper were treated in the same way. The *in situ* XRD measurement was carried out at beamline X18A at the NSLS at BNL using a wide-angle PSD. The data collection time of the each scan was 5 min. The dips at about 60° 2θ angle in the XRD patterns of Figs. 2–4 are caused by the defect of the PSD detector. It is marked as glitch and should be disregarded. Because the cubic $LiMn_2O_4$ spinel structure is well known, only Bragg peaks of $(1\,1\,1)_C$, $(5\,1\,1)_C$, $(4\,4\,0)_C$ and $(5\,3\,1)_C$ are shown in Fig. 1(b). During the first charge, all Bragg peaks continuously shift to higher 2θ angles, indicating the contraction of lattice parameter of the cubic unit cell. The lattice parameter of the cubic unit cell calculated by the least-square fitting contracted from 8.20 Å to 8.05 Å during first charge. The phase transition from cubic 1 to cubic 2 can be observed from scans 17 to 29 and that from cubic 2 to cubic 3 takes place from scans 41 to 65. These results are in good agreements with our previous publications [15,16]. When charged above 4.5 V, neither the position nor the shape of each Bragg peak for the cubic 3 phase exhibits any changes at all. Since no further structural changes in the $LiMn_2O_4$ spinel were observed, the apparent charge capacity accumulated from scans 73 to 84 at the end of the charge (near 5.0 V) in Fig. 1(a) is attributed to the electrolyte decomposition.

Fig. 2(a) and (b) shows the first charge curve of $LiNi_{1/3}Co_{1/3}Mn_{1/3}O_2$ cathode charged to 5.2 V *vs.* Li/Li^+ and *in situ* XRD patterns collected during first charge respectively. Measured up to 4.8 V, the charge capacity of the $LiNi_{1/3}Co_{1/3}Mn_{1/3}O_2$ cathode is 223 mAh g^{-1}. Bragg peaks of $(0\,0\,3)_H$, $(1\,0\,7)_H$, $(1\,0\,8)_H$, $(1\,1\,0)_H$ and $(1\,1\,3)_H$ for hexagonal layered phase were selectively shown in Fig. 2(b). The peaks in the XRD patterns can be indexed to two hexagonal phases (H1 and H2) similar to those indexed by Yang et al. for $LiNiO_2$ and $LiNi_{0.8}Co_{0.15}Al_{0.05}O_2$ [17,18]. At the beginning

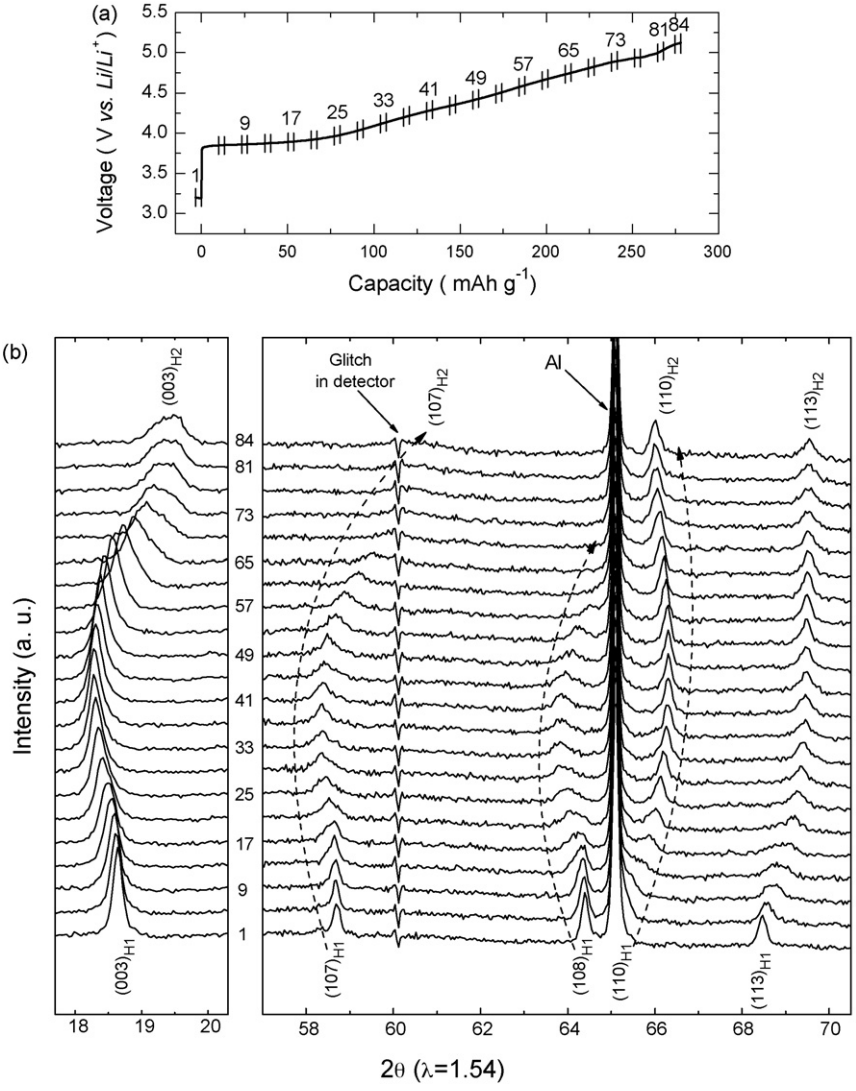

Fig. 2. (a) First charge curve of $LiNi_{1/3}Co_{1/3}Mn_{1/3}O_2$ cathode in the Li-half cell at C/7 rate, and (b) corresponding *in situ* XRD patterns.

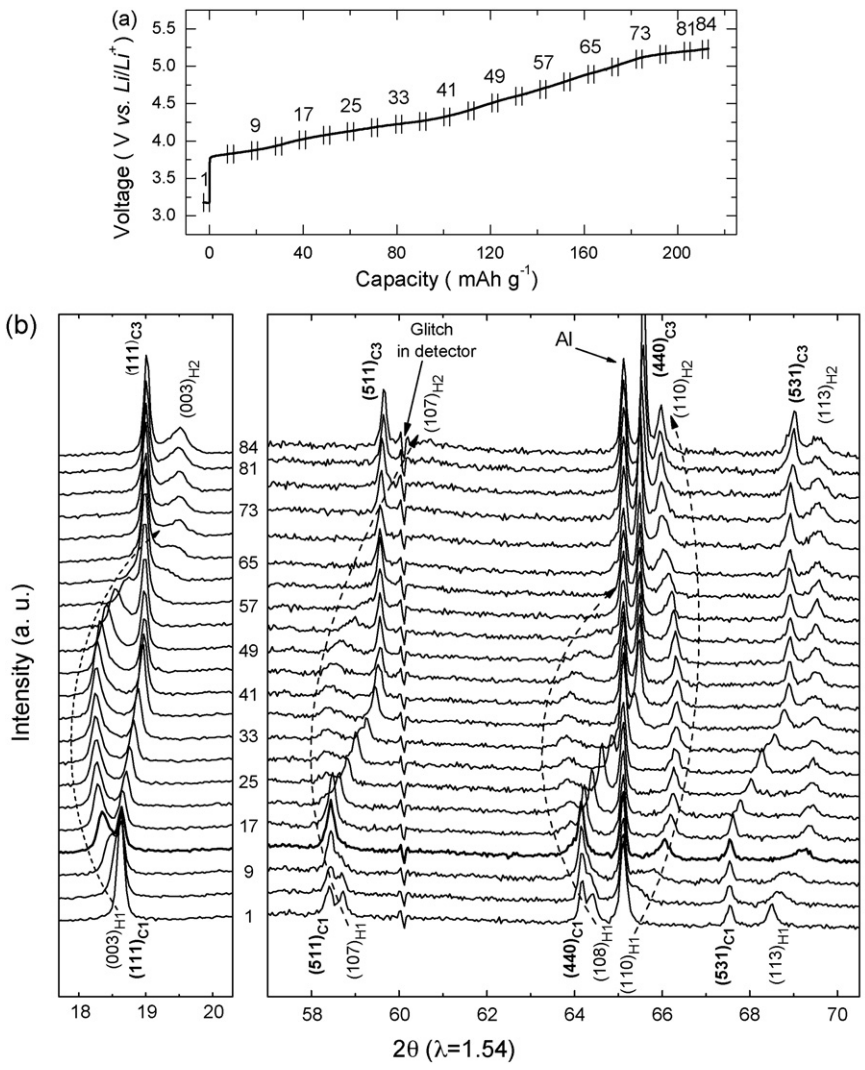

Fig. 3. (a) First charge curve of $LiMn_2O_4$–$LiNi_{1/3}Co_{1/3}Mn_{1/3}O_2$ composite cathode in the Li-half cell at C/7 rate, and (b) corresponding *in situ* XRD patterns.

of charge, the (0 0 3) peak shifts to lower 2θ angle positions (scans 1–37) and then moves back to higher 2θ angle positions during further charge (scans 41–84), indicating an expansion of *c*-axis first and then followed by a contraction of *c*-axis. On the other hand, the (1 1 0) peak position, which is sensitive only to the changes in the length of *a*- or *b*-axes in the unit cell, shifts toward higher 2θ angles in the early stage of charge (scans 1–37), and then shifts to lower 2θ angles very slightly during further charge (scans 41–84), indicating a contraction of *a*- and *b*-axes first and followed by a very slight expansion of *a*- and *b*-axes during the late stage of charge. The structural changes for $LiNi_{1/3}Co_{1/3}Mn_{1/3}O_2$ during the first charge are quite similar with our previous studies on the same system [18].

Fig. 3(a) shows the first charge curve of the $LiMn_2O_4$–$LiNi_{1/3}Co_{1/3}Mn_{1/3}O_2$ composite cathode with a cut-off voltage of 5.2 V *vs.* Li/Li^+ using a constant current charge at a C/7 rate. The voltage profile of the $LiMn_2O_4$–$LiNi_{1/3}Co_{1/3}Mn_{1/3}O_2$ composite cathode shows continuous increase in potential up to 5.2 V, combining the features of two components (i.e., $LiMn_2O_4$ and $LiNi_{1/3}Co_{1/3}Mn_{1/3}O_2$). Measured up to 4.8 V, the capacity of the $LiMn_2O_4$–$LiNi_{1/3}Co_{1/3}Mn_{1/3}O_2$ composite cathode is 153 mAh g^{-1} which is quite close to the average value of 116 mAh g^{-1} and 223 mAh g^{-1} for spinel $LiMn_2O_4$ and layered $LiNi_{1/3}Co_{1/3}Mn_{1/3}O_2$, respectively. Based on the different crystal structure of the spinel $LiMn_2O_4$ and layered $LiNi_{1/3}Co_{1/3}Mn_{1/3}O_2$, *in situ* XRD data can provide valuable information about the Li extraction behaviors of each component in the $LiMn_2O_4$–$LiNi_{1/3}Co_{1/3}Mn_{1/3}O_2$ composite cathode during the first charge.

In situ XRD patterns of the $LiMn_2O_4$–$LiNi_{1/3}Co_{1/3}Mn_{1/3}O_2$ composite cathode collected at certain potential ranges are plotted in Fig. 3(b). Bragg peaks corresponding to both spinel $LiMn_2O_4$ and layered $LiNi_{1/3}Co_{1/3}Mn_{1/3}O_2$ phases were clearly observed in the *in situ* XRD patterns. The peaks indexed as $(1\,1\,1)_C$, $(5\,1\,1)_C$, $(4\,4\,0)_C$ and $(5\,3\,1)_C$ are for cubic spinel phase, and the $(0\,0\,3)_H$, $(1\,0\,7)_H$, $(1\,0\,8)_H$, $(1\,1\,0)_H$ and $(1\,1\,3)_H$ are originated from hexagonal phase of the layered component. In general, the variations of *in situ* XRD peaks for both cubic spinel and hexagonal layered components during charge show similar trends as observed in the *in situ* XRD patterns of each component during the first charge as in Figs. 1(b) and 2(b). However, we would like to point out some interesting features observed in the *in situ* XRD patterns of the $LiMn_2O_4$–$LiNi_{1/3}Co_{1/3}Mn_{1/3}O_2$ composite cathode during charge. At the beginning of charge (scans 1–13), while the Bragg peaks of $LiNi_{1/3}Co_{1/3}Mn_{1/3}O_2$ start to move to different 2θ angles with increased charge capacity, the Bragg peaks corresponding to $LiMn_2O_4$ remain unchanged until the cell voltage reaches ~3.9 V (where the XRD pattern is plotted in thicker line in Fig. 3(b)). From scans 17 to 41, the structure changes are dominated by the $LiMn_2O_4$ component. During this region (scans 17–41), the XRD peaks corresponding to hexagonal component do not have much changes in their 2θ positions at all. After that, from scans 45

to 84, the Bragg peaks for the layered component keep moving until the end of charge. Other interesting feature is that the Bragg peaks for spinel phase shift slightly to higher 2θ angles near the end of charge from scans 73 to 84, indicating a slight contraction of the lattice constant of cubic unit cell.

From the above *in situ* XRD results, two important factors determining which component is more active than the other in a certain voltage range can be identified: the voltage thresholds of phase transition and the rate capability. For example, the phase transition of the $LiMn_2O_4$ component does not take place at the beginning of the charge because the cell voltage is lower than the 4.0 V thresholds for lithium extraction from this component. Therefore, the lithium extraction takes place from the layered $LiNi_{1/3}Co_{1/3}Mn_{1/3}O_2$ component only when the voltage is below 4.0 V *vs.* Li/Li^+. However, when the cell voltage reaches the thresholds of $LiMn_2O_4$ at ~4.0 V, both components become active, but the lithium extraction from the spinel $LiMn_2O_4$ component is much more than that from the $LiNi_{1/3}Co_{1/3}Mn_{1/3}O_2$ component. This is attributed to the higher rate capability in addition to the voltage threshold of $LiMn_2O_4$ spinel component.

In order to make a clear comparison of the structural changes of the single $LiMn_2O_4$, $LiNi_{1/3}Co_{1/3}Mn_{1/3}O_2$, and the $LiMn_2O_4$–$LiNi_{1/3}Co_{1/3}Mn_{1/3}O_2$ composite cathode during the first charge, the lattice parameters were calculated using least-square fitting and plotted in Fig. 4 as a function of the charge capacity. Standard deviation of the least squire fitting of the lattice parameters is marked using error bars at each point. The lattice parameters for the $LiMn_2O_4$ during charge show continuous contraction of the cubic spinel unit cell. On the other hand, the lattice parameters of the $LiNi_{1/3}Co_{1/3}Mn_{1/3}O_2$ show an initial expansion along the *c*-axis and a simultaneous contraction along the *a*- and *b*-axis during early stage of charge. Towards the end of charge, there is a major contraction along the *c*-axis and a slight expansion along the *a*- and *b*-axis. The lattice parameter changes of the $LiMn_2O_4$ and $LiNi_{1/3}Co_{1/3}Mn_{1/3}O_2$ during charge agrees well with the previous results [15,18]. Based on the lattice parameter changes of each component, the charge process of $LiMn_2O_4$–$LiNi_{1/3}Co_{1/3}Mn_{1/3}O_2$ composite cathode can be divided into 4 regions as plotted in Fig. 4. In region I (0–27 mAh g^{-1} charge capacity), the lattice parameter of $LiMn_2O_4$ component remains unchanged while the *a*- and *c*-axes of the $LiNi_{1/3}Co_{1/3}Mn_{1/3}O_2$ component changes continuously. In region II (27–85 mAh g^{-1} charge capacity) a significant contraction occurs in the spinel cubic lattice parameter with the magnitude closer to the single $LiMn_2O_4$ component cathode. On the other hand, in this region II, the *a*- and *c*-axes of the $LiNi_{1/3}Co_{1/3}Mn_{1/3}O_2$ component show only slight changes with a less magnitude as those in single $LiNi_{1/3}Co_{1/3}Mn_{1/3}O_2$ component cathode at same charge capacity. In region III (85–175 mAh g^{-1} charge capacity), the lattice parameter changes are observed only in the $LiNi_{1/3}Co_{1/3}Mn_{1/3}O_2$ component, indicating a slight expansion along the *a*-axis and major contraction along the *c*-axis. At the end of the charge, slight further lattice contraction of the spinel unit cell is observed in region IV (175–215 mAh g^{-1} charge capacity), whereas the lattice parameters for the $LiNi_{1/3}Co_{1/3}Mn_{1/3}O_2$ remain unchanged. This slight lattice parameter change of $LiMn_2O_4$ in region IV tells us that the charge obtained up to ~5.2 V is real in the $LiMn_2O_4$–$LiNi_{1/3}Co_{1/3}Mn_{1/3}O_2$ composite cathode. This is quite different than that in the case of single $LiMn_2O_4$ component cathode, where the apparent capacity near 5.0 V is attributed to the electrolyte decomposition. This result is quite interesting. It shows that when mixed with layer structured component, the $LiMn_2O_4$ has the potential to be charged to a voltage as high as 5.2 V without causing significant electrolyte decomposition suggesting that it will have great impact in the development of high voltage lithium battery research, where the doped $LiMn_{2-x}M_xO_4$ (M = Co, Ni, and Cu) are considered as high voltage cathode candidates.

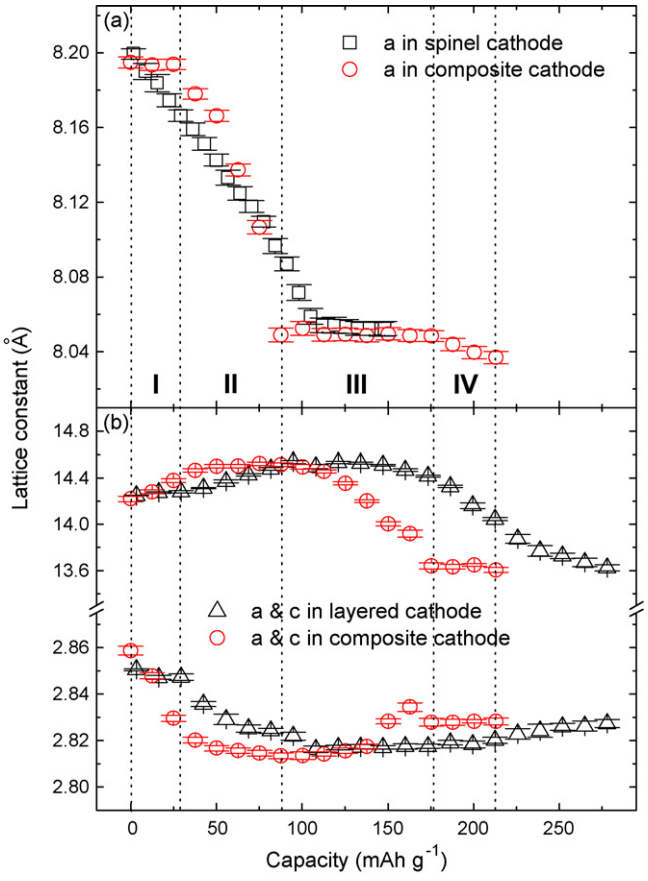

Fig. 4. Variations of the lattice parameters of $LiMn_2O_4$, $LiNi_{1/3}Co_{1/3}Mn_{1/3}O_2$ and $LiMn_2O_4$–$LiNi_{1/3}Co_{1/3}Mn_{1/3}O_2$ composite cathodes in the Li-half cell during the first charge.

In order to examine the structural changes of $LiMn_2O_4$–$LiNi_{1/3}Co_{1/3}Mn_{1/3}O_2$ composite cathode in a Li-ion cell, the pouch-type Li-ion cell using $LiMn_2O_4$–$LiNi_{1/3}Co_{1/3}Mn_{1/3}O_2$ composite as cathode and MCMB as anode materials was fabricated by LG Chem. for *in situ* XRD measurements. The capacity of the pouch cell was designed to 10 mAh within the operating voltage of 2.5–4.2 V which is similar to the operating condition of most of the commercial cells. The pre-charged cell was discharged at a C/2 rate first, rested at open circuit potential (OCP) for 30 min, and then recharged at a C2/rate. Fig. 5 shows the discharge/charge curves of the pouch cell during the *in situ* XRD measurements. The pouch cell delivered discharge and charge capacities of 10.3 mAh and 9.9 mAh, respectively. *In situ* XRD patterns were continuously collected every 3 min during discharge/charge. The corresponding *in situ* XRD patterns of the pouch cell are plotted in Fig. 6. The *in situ* XRD measurement was carried out at beamline X7B at the NSLS at BNL using a Mar-345 image plate detector. The XRD patterns marked as #1 and #2 correspond to the beginning and ending of the discharge process respectively, while the #3 and #4 patterns are corresponding to where the charge current was supplied and cut-off respectively. Similarly to the *in situ* XRD patterns of the $LiMn_2O_4$–$LiNi_{1/3}Co_{1/3}Mn_{1/3}O_2$ composite cathode in Li-half cell in Fig. 3(b), Bragg peaks for both spinel $LiMn_2O_4$ and layered $LiNi_{1/3}Co_{1/3}Mn_{1/3}O_2$ phases were clearly seen in the *in situ* XRD patterns of the pouch cell. The peaks indexed as S(1 1 1), S(5 1 1), S(4 4 0) and S(5 3 1) are for cubic spinel phase, and those indexed as L(0 0 3), L(1 0 7), L(1 0 8), L(1 1 0) and L(1 1 3) are for hexagonal layered phase. As the cell starts to discharge, the Bragg peaks corresponding to the spinel phase move continuously to lower 2θ angles while the Bragg peaks for the layered

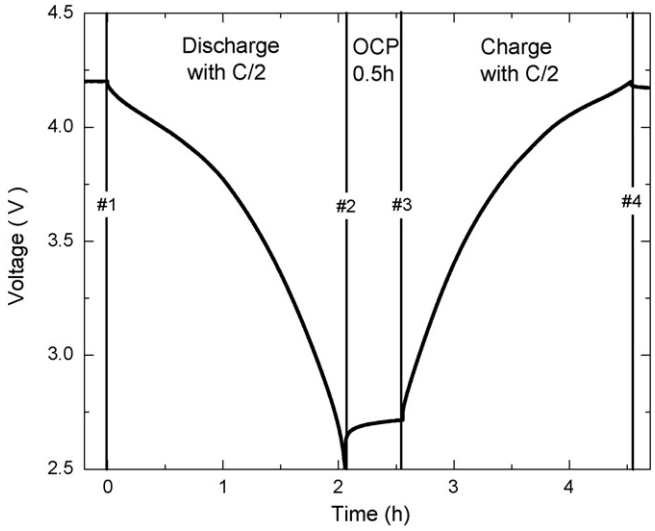

Fig. 5. Discharge/charge curves of the pouch-type Li-ion cell composed of $LiMn_2O_4$–$LiNi_{1/3}Co_{1/3}Mn_{1/3}O_2$ composite cathode and MCMB anode at C/2 rate. Voltage window: 2.5–4.2 V.

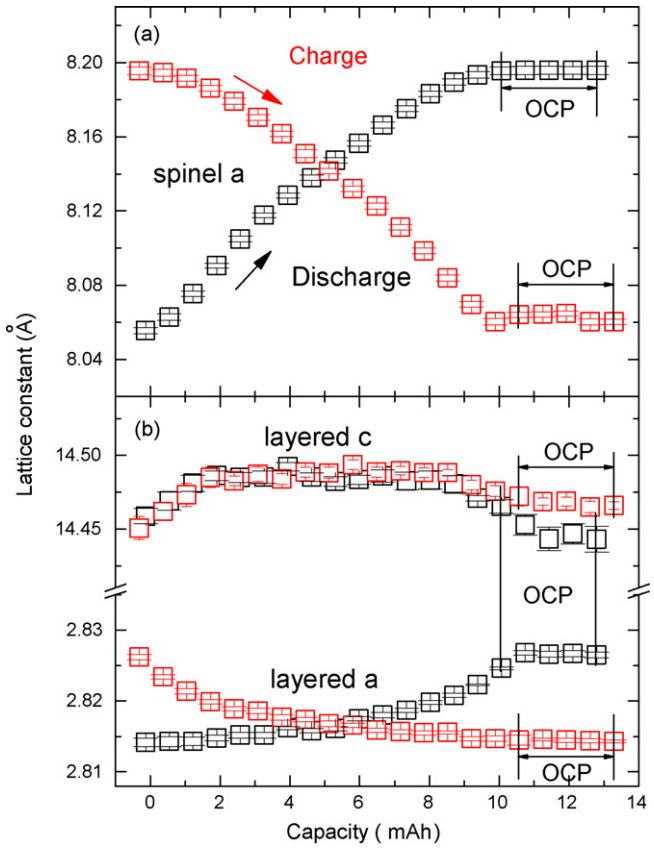

Fig. 7. Variations of the lattice parameters of the $LiMn_2O_4$–$LiNi_{1/3}Co_{1/3}Mn_{1/3}O_2$ composite cathode in the pouch-type Li-ion cell during discharge/charge.

phase remains unchanged. As the discharge proceeds to ~3.62 V, the layered L(1 1 0) and L(1 1 3) peaks start to shift to lower 2θ angles and keep moving until the end of discharge. The peak shifts of the spinel component become slowed down when the discharge process is closing to the end. During the following charge, both spinel peaks and layered peaks shift back to their original positions showing good reversibility. Comparing to the *in situ* XRD patterns for the $LiMn_2O_4$–$LiNi_{1/3}Co_{1/3}Mn_{1/3}O_2$ composite cathode in the Li-half cell (Fig. 3(b)), where the structural changes of layered and spinel are equally significant, the structural changes in the pouch-type Li-ion cell are dominated by the spinel phase, with much less changes in the layered component. This is mainly caused by the voltage range of the discharge–charge cycling for the Li-ion cell and tells us that the main contribution to the capacity comes from the spinel phase, if the 2.5–4.2 V voltage range is selected. The changes of lattice parameters during discharge/charge are plotted in Fig. 7. The lattice parameter of spinel phase expands from 8.06 Å to 8.20 Å during discharge, and reversibly changes back to its original value during the following charge. The lattice parameter changes of the layered phase also show reversible behaviors during discharge and charge of the Li-ion cell as seen in Fig. 7(b). Similar to the lattice parameter changes in the Li-half cell (Fig. 4), when the lattice parameters *a* and *c* start to change towards the end of discharge (and at the beginning of charge) the lattice parameter changes for the spinel

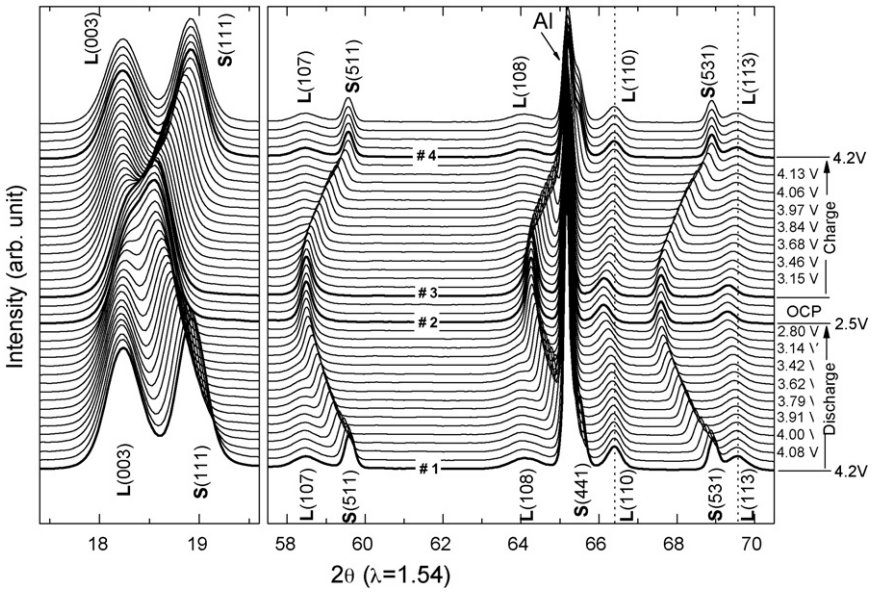

Fig. 6. *In situ* XRD patterns of the pouch-type Li-ion cell during discharge/charge. Pattern #1: before discharge; pattern #2: after discharge; pattern #3: before charge; pattern #4: after charge.

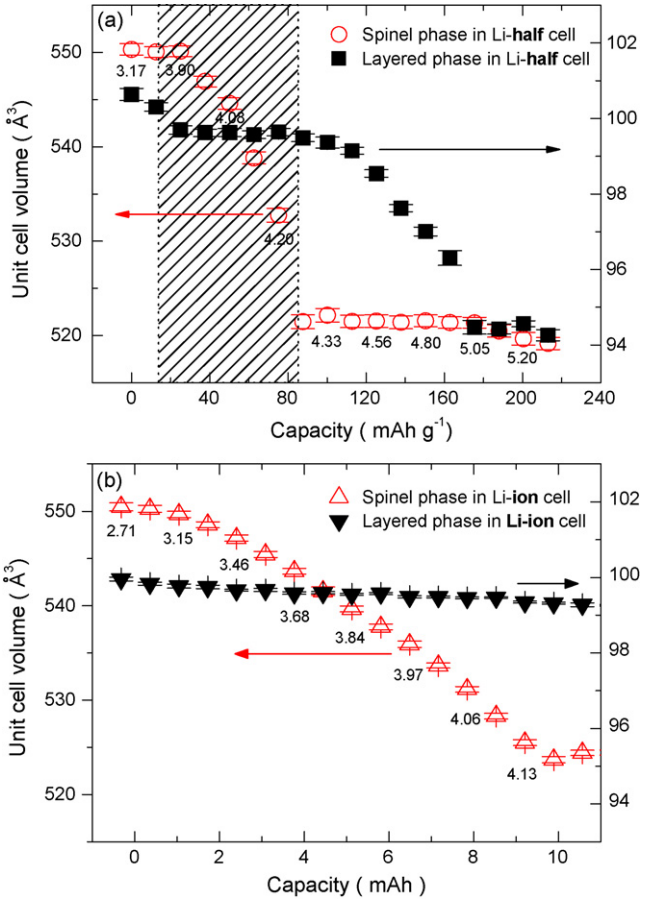

Fig. 8. Variations of the unit cell volumes of the $LiMn_2O_4$–$LiNi_{1/3}Co_{1/3}Mn_{1/3}O_2$ composite cathode in (a) the Li-half cell and (b) pouch-type Li-ion cell during charge. Shaded region is marked out in (a) to show the corresponding utilization of $LiMn_2O_4$–$LiNi_{1/3}Co_{1/3}Mn_{1/3}O_2$ composite cathode in the pouch-type Li-ion cell. The numbers marked on the graphs correspond to the cell voltages.

component slow down at the end of discharge (and are not significant at the beginning of charge) in the pouch-type Li-ion cell in Fig. 7. However, there is a difference in the lattice parameter changes of the layered component in the Li-half cell and pouch-type Li-ion cell. Compared to the lattice parameter changes of the $LiMn_2O_4$–$LiNi_{1/3}Co_{1/3}Mn_{1/3}O_2$ composite cathode in the Li-half cell in Fig. 4, the $LiNi_{1/3}Co_{1/3}Mn_{1/3}O_2$ component in the pouch-type Li-ion cell shows much less structural changes in its lattice parameters for *a*- and *c*-axes.

Since the changes of *a* and *b* lattice parameters of layered phases are in the opposite directions, making it hard to compare with the changes of cubic spinel phase, the changes in unit cell volume will give a better comparison. These changes can provide comprehensive information about the contribution of each component to the capacity at different charge–discharge states. The unit cell volume changes *vs.* the charging capacity of the spinel and layered components in the Li-half cell and pouch-type Li-ion cell are plotted in Fig. 8(a) and (b), respectively. The mAh g^{-1} unit is used for *x*-axis in Fig. 8(a) for the Li-half cell, while mAh unit is used for the pouch-type Li-ion cell in Fig. 8(b). The contraction of unit cell volume in the Li-half cell takes place in an alternative fashion during charge, starts with the layered, follows by the spinel, and finally ends with very small moves in both spinel and layered phases. The unit cell volume changes (ΔV) of the spinel and layered components in the Li-half cell before and after charge are 28.84 $Å^3$ for the spinel and 6.38 $Å^3$ for the layered. On the other hand, the unit cell volume for the layered component in the pouch-type Li-ion cell shows much less changes (i.e., $\Delta V = 0.68$ $Å^3$) than that in the Li-half cell during charge. In case of the spinel component in the pouch-type Li-ion cell, the total volume change during charge is 26.80 $Å^3$ which is quite close of the volume change in the Li-half cell. This result reveals that major contribution to the capacity of the pouch-type Li-ion cell is attributed to the spinel component. Since the cut-off voltage of the Li-half cell (i.e., ~5.2 V *vs.* Li/Li^+) and pouch-type Li-ion cell (i.e., 4.2 V *vs.* MCMB anode) are quite different, the less structural change of the layered component in the pouch-type Li-ion cell during charge is mainly caused by the smaller utilization of the composite cathode in the pouch-type Li-ion cell. Gauged by the unit cell volume changes in the Li-half cell and pouch-type Li-ion cell in Fig. 8(a) and (b), a shaded region is marked out in Fig. 8(a) to show the corresponding utilization of $LiMn_2O_4$–$LiNi_{1/3}Co_{1/3}Mn_{1/3}O_2$ composite cathode in the pouch-type Li-ion cell.

From the *in situ* XRD results of this study, valuable information for optimizing cathode composition can be derived. If the desired voltage operation range is between 2.5 V and 4.2 V, increasing the percentage of $LiMn_2O_4$ spinel component will increase the capacity, since the contribution of layered $LiNi_{1/3}Co_{1/3}Mn_{1/3}O_2$ component is quite small in this voltage range. In order to fully utilize the contribution of the layered component, a higher cut-off voltage is required. Therefore, if the more stable electrolytes at higher voltages can be developed, the advantages of the high capacity from the layered component and the high rate from the spinel can be utilized at the same time.

4. Conclusions

During the first charge up to ~5.2 V *vs.* Li/Li^+, the *in situ* XRD spectra for the $LiMn_2O_4$–$LiNi_{1/3}Co_{1/3}Mn_{1/3}O_2$ composite cathode in the Li-half cell tracked the structural changes of each component. At the early stage of charge, the lithium extraction and structural changes take place in the $LiNi_{1/3}Co_{1/3}Mn_{1/3}O_2$ component only. When the cell voltage reaches at ~4.0 V *vs.* Li/Li^+, lithium extraction from the spinel $LiMn_2O_4$ component starts and becomes the major contributor for the cell capacity due to the higher rate capability in addition to the voltage threshold of $LiMn_2O_4$. These results show that both the voltage thresholds and the rate capability of each component are quite important factors in determining the structural changes. When the voltage passed 4.3 V, the major structural changes are from the $LiNi_{1/3}Co_{1/3}Mn_{1/3}O_2$ component, while the $LiMn_2O_4$ component is almost unchanged. At the end of the charge (5.0–5.2 V *vs.* Li/Li^+), a slightly further lattice contraction of the spinel unit cell was observed, which is quite different than that in the case of single $LiMn_2O_4$ component cathode, where no structural changes of the cathode were observed and the apparent capacity near 5.0 V was attributed to the electrolyte decomposition. This might be an implication of the suppressing effect on the electrolyte decomposition at high voltage (5 V) benefited from mixing $LiMn_2O_4$ with layer structured component.

In the Li-ion cell using a MCMB anode and a composite cathode cycled between 2.5 V and 4.2 V, the structural changes are dominated by the spinel $LiMn_2O_4$ component, with much less changes in the layered $LiNi_{1/3}Co_{1/3}Mn_{1/3}O_2$ component, comparing with the Li-half cell results. This is attributed to the use of lower cut-off voltage used for the Li-ion cell (e.g., 5.2 V for Li-half cell *vs.* 4.2 V for Li-ion cell). The *in situ* XRD results of this study suggest that if the desired voltage operation range of Li-ion cell is between 2.5 V and 4.2 V, increasing the percentage of $LiMn_2O_4$ spinel component will increase the capacity, since the contribution of layered $LiNi_{1/3}Co_{1/3}Mn_{1/3}O_2$ component is quite small in this voltage range. In order to fully utilize the contribution of the layered component, a higher cut-off voltage is required. Therefore, if electrolytes with better stability at higher voltages can be developed, the advantages

of the high capacity from the layered component and the high rate from the spinel can be utilized at the same time.

Acknowledgements

The work at BNL was supported by the Assistant Secretary for Energy Efficiency and Renewable Energy, Office of Vehicle Technologies, under the program of "Hybrid and Electric Systems", of the U.S. Department of Energy under Contract Number DEAC02-98CH10886. This work was supported by the new faculty research program 2008 of Kookmin University in Korea. This work was also supported by the Korea Research Foundation Grant funded by the Korean Government (MOEHRD, Basic Research Promotion Fund) (KRF-2008-331-D00248). We acknowledge financial supports from the NRL Programs (R0A-2007-000-20105-0), and the CMPS (R11-2005-048-00000-0) of MEST/KOSEF.

References

[1] T. Numata, C. Amemiya, T. Kumeuchi, M. Shirakara, M. Yonezawa, J. Power Sources 97–98 (2001) 358–360.
[2] Z.F. Ma, X.Q. Yang, X. Sun, J. McBreen, J. New Mater. Electrochem. Syst. 4 (2001) 121–125.
[3] Z.F. Ma, X.Q. Yang, X.Z. Liao, X. Sun, J. McBreen, Electrochem. Commun. 3 (2001) 425–428.
[4] H. Kitao, T. Fujihara, K. Takeda, N. Nakanishi, T. Nohma, Electrochem. Solid-State Lett. 8 (2005) A87–A90.
[5] S.T. Myung, M.H. Cho, H.T. Hong, T.H. Kang, C.S. Kim, J. Power Sources 146 (2005) 222–225.
[6] A. Manthiram, W. Choi, Electrochem. Solid-State Lett. 10 (2007) A228–A231.
[7] J.F. Whitacre, K. Zaghib, W.C. West, B.V. Ratnakumar, J. Power Sources 177 (2008) 528–536.
[8] J. Baker, M. Saudi, K. Yazid, E. Tracy, US Patent 7,041,239 (2006).
[9] M.M. Thackeray, Prog. Solid State Chem. 25 (1997) 1–71.
[10] Y. Xia, Y. Zhou, M. Yoshio, J. Electrochem. Soc. 144 (1997) 2593–2600.
[11] Z. Lu, D.D. MacNeil, J. Dahn, Electrochem. Solid-State Lett. 4 (2002) A200–A203.
[12] N. Yabuuchi, T. Ohzuku, J. Power Sources 119–121 (2003) 171–174.
[13] K.M. Shaju, G.V. Subba Rao, B.V.R. Chowdari, Electrochim. Acta 48 (2002) 145–151.
[14] I. Belharouak, Y.K. Sun, J. Liu, K. Amine, J. Power Sources 123 (2003) 247–252.
[15] X.Q. Yang, X. Sun, S.J. Lee, J. McBreen, S. Mukerjee, M.L. Daroux, X.K. Xing, Electrochem. Solid-State Lett. 2 (1999) 157–160.
[16] K.Y. Chung, H.S. Lee, W.S. Yoon, J. McBreen, X.Q. Yang, J. Electrochem. Soc. 153 (2006) A774–A780.
[17] X.Q. Yang, X. Sun, J. McBreen, Electrochem. Commun. 2 (2000) 733–737.
[18] W.S. Yoon, K.Y. Chung, J. McBreen, X.Q. Yang, Electrochem. Commun. 8 (2006) 1257–1262.